Measurement of the ^{10}B(p,α_{0})^{7}Be cross section from 5 keV to 1.5 MeV in a single experiment using the Trojan horse method

C. Spitaleri *et al.*

Phys. Rev. C **95**, 035801 — Published 1 March 2017

DOI: 10.1103/PhysRevC.95.035801

First time measurement of the ^{10}B$(p,\alpha_0)^7$Be cross section from 5 keV to 1.5 MeV in a single experiment dusing the Trojan Horse Method

C. Spitaleri[1,2], S.M.R. Puglia[2], M. La Cognata[2], L. Lamia[1], S. Cherubini[1,2], A. Cvetinović[2], G. D'Agata[1,2], M. Gulino[2,3], L. Guardo[2], I. Indelicato[2], R.G. Pizzone[2], G.G. Rapisarda[1,2], S. Romano[1,2], M.L. Sergi[2], R. Spartá[2], S.Tudisco[2], A. Tumino[2,3]
[1]*Dipartimento di Fisica e Astronomia, University of Catania, Catania, Italy.*
[2]*INFN-Laboratori Nazionali del Sud, Catania, Italy.*
[3]*Facoltá di Ingegneria e Architettura, "Kore" University, Enna, Italy.*[*]

M. Gimenez Del Santo, N. Carlin, M. G. Munhoz, F. A. Souza, and A. Szanto de Toledo[†]
Departamento de Fisica Nuclear,
Universitade de Sao Paulo, Sao Paulo, Brasil.
[†]*Deceased.*

A. Mukhamedzhanov
Cyclotron Institute, Texas A&M University, College Station, TX 77843, USA.

C. Broggini[1], A. Caciolli[1,2], R. Depalo[1,2], R. Menegazzo[1], V. Rigato[3]
[1]*INFN-Padova, Padova, Italy.*
[2]*Dipartimento di Fisica,*
University of Padova, Padova, Italy.
[3]*INFN-Laboratori Nazionali di Legnaro, Legnaro,Italy.*

I. Lombardo, D. Dell'Aquila
Dipartimento di Fisica, University of Napoli, Napoli, Italy.
INFN-Napoli, Napoli, Italy.
(Dated: January 24, 2017)

For the first time the astrophysical factor of the ^{10}B$(p,\alpha_0)^7$Be reaction has been measured over a wide energy range, from 5 keV to 1.5 MeV, via the Trojan Horse Method (THM) applied to the quasi-free ^{2}H(^{10}B,α^7Be)n reaction. Therefore, the $S(E)$-factor has been recast into absolute units by scaling in the energy range 200 keV - 1.2 MeV to a recent measurement using the activation method, leading to a normalization uncertainty of 4%. An R-matrix fit of the THM data was performed, to parameterize the S-factor, obtain spectroscopic information on the populated resonances, and compare with other recent experiments. Finally, a new determination of the screening potential U_e has been obtained, U_e=240±50 eV, with a much smaller error than our previous measurement.

I. INTRODUCTION

The ^{10}B$(p,\alpha)^7$Be reaction at low energy is of interest for nuclear physics, nuclear astrophysics and applied physics. In nuclear physics, it allows one to investigate ^{11}C states presently poorly known [1, 2]. In nuclear astrophysics, it represents the main ^{10}B destruction channel in H-rich main-sequence star outer layers. Therefore, its cross section, dominated by a resonance at 10 keV (due to the $J^\pi = \frac{5}{2}^+$ 8.699 MeV ^{11}C level), corresponding to the Gamow window energy (E_G= 10±5 keV) for such stellar environments [3], plays a key role in predicting boron abundances and constraining mixing phenomena occurring in such stars [4]. Finally, the ^{10}B$(p,\alpha)^7$Be reaction is important for application to clean energy production in future generation fusion reactors. In this framework, proton-induced reactions on natural boron ^{nat}B, containing ^{11}B isotopes ($\backsim$80%) and ^{10}B isotopes ($\backsim$20%), have been considered as possible candidates for fusion processes with no neutron emissions [5, 6]. If ^{nat}B is used as fuel, the ^{10}B$(p,\alpha_0)^7$Be reaction can be a source of radioactive waste in the reactors, due to the production of ^{7}Be ($\tau_{1/2}$=53.22±0.06 d), thus influencing future fusion reactor building projects.

The ^{10}B$(p,\alpha)^7$Be reaction at low energy exhibits two different exit channels, i.e. $^{10}B(p,\alpha_0)^7$Be and ^{10}B$(p,\alpha_1)^7$Be. However, because of the Coulomb penetrability in the outgoing channel and for phase-space considerations, at low bombarding energies ($E_p \leq$ 1 MeV) the α_1 channel is strongly suppressed with respect to the α_0 one.

For all the reasons discussed so far, it is important to have good quality data of the ^{10}B$(p,\alpha)^7$Be cross section at low bombarding energies. The cross section of the ^{10}B$(p,\alpha_0)^7$Be reaction has been investigated in many different experiments, direct [7–13] and indirect [14–16], and it has been calculated using DWBA and potential model [17]. Reviews of the data are reported in [18, 19].

[*] e-mail: spitaleri@lns.infn.it

However, none of these experiments provides a complete and consistent measurement of the cross section over the energy range of interest for nuclear physics, nuclear astrophysics and applied physics, about 0-1 MeV, where at least six excited levels of ^{11}C in the 8.7-9.7 MeV excitation energy range contribute to the cross section. These problems have triggered two recent direct measurements of the ^{10}B(p,α)^{7}Be cross section. In the first measurement by Caciolli et al. [13], the total cross section has been measured by means of the activation technique. Experimental data cover a wide center of mass energy range, from 300 to 1200 keV, and few points (about 10) with very high precision and accuracy were taken. The dataset thus obtained shows a large discrepancy with respect to previous data at the same energies and a total uncertainty reduced to the level of 6%. On the contrary, Lombardo et al. [12] measured the ^{10}B(p,α_0)^{7}Be at many energies in a small energy range, between about 500 keV and 1 MeV, using the inverse absorber technique. New resonances were pointed out by the authors, who performed a very accurate R-matrix analysis even if for experimental reasons they could not approach the energy range of astrophysical importance.

An indirect measurement was also attempted few years ago by means of the Trojan Horse Method (THM) [20–22], aiming at solving the inconsistencies among direct measurements [16]. The THM is a renowned indirect method, very useful in the study of reaction with charged particles in the exit channel, in contrast with ANC [23] and Coulomb dissociation [24], focused on radiative capture reactions. However, the ^{10}B(p,α_0)^{7}Be cross section was measured in the energy range 0-100 keV [16], and the lack of a sufficient statistics did not allow us to extend the excitation function in the region 100 -1000 keV. Normalization was then performed by matching the THM S-factor to a R-matrix calculation performed by introducing into the calculation the resonance parameters from the literature [25], and caused the measured $S(E)$-factor to be affected by an uncertainty of 20% mainly due to the normalization procedure [16].

The present paper reports on a new measurement of the ^{10}B(p,α_0)^{7}Be reaction with the THM applied to the ^{2}H(^{10}B,α_0^{7}Be)n process in the energy range 5 keV to 1.5 MeV. We focus on the α_0 channel that is the dominant one in the energy range of interest [17]. Having a unique set of precise data over such a wide energy range and given the availability of new precise data from [12, 13] for normalization, this work definitely improves our knowledge of the ^{10}B(p,α_0)^{7}Be reaction over the whole energy range of interest.

II. BASIC THEORY

The study of the ^{2}H(^{10}B,α_0^{7}Be)n nuclear reaction to extract the ^{10}B(p,α_0)^{7}Be two-body reaction has been performed within the Plane Wave Impulse Approximation (PWIA) framework. The motivations for such a simplified approach in the application of the THM are discussed in several previous papers (see for example ref [22, 26]. Some basic features of this simplified approach are presented here. More sophisticated theoretical formulations can be found in [22].

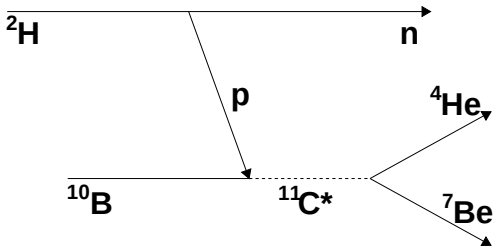

FIG. 1. Diagram representing the quasi-free process ^{2}H+^{10}B→α+^{7}Be+n. The upper vertex describes the virtual decay of the THM-nucleus ^{2}H into the participant p and spectator n to the p+^{10}B→α+^{7}Be reaction that takes place in the lower vertex.

A. Quasi-free reaction

The ^{2}H(^{10}B,α_0^{7}Be)n measurement has been performed in inverse kinematics using a deuteron to transfer the participant proton. The quasi-free (QF) contribution (see e.g. [27] and references therein) to the ^{2}H(^{10}B,α_0^{7}Be)n three-body reaction, performed at energy well above the Coulomb barrier in the ^{2}H+^{10}B entrance channel, is selected to extract the ^{10}B(p,α_0)^{7}Be cross section at astrophysical energies free of Coulomb suppression and electron screening (bare-nucleus cross section). If the process can be described as QF, the reaction mechanism can be sketched using the diagram in Fig.1 (pole approximation), while other graphs (triangle graphs) indicating rescattering between the reaction products are neglected [28–30]. In QF dynamics, ^{10}B interacts only with the participant proton while the neutron acts like a spectator to the ^{1}H(^{10}B,α_0)^{7}Be virtual reaction. The QF process can be regarded as a particular class of transfer reactions to the continuum. The experiment kinematical conditions were selected to explore the phase space region where the QF contribution is expected to be dominant. In the data analysis, only QF events are selected and other reaction mechanisms, yielding the same particles in the exit channel such as sequential decay (SD) or direct breakup (DBU) were identified and subtracted, if any.

In the impulse approximation (IA), the cross section of the ^{2}H(^{10}B,α_0^{7}Be)n QF reaction can be factorized into two terms corresponding to the vertices of Fig.1, besides a phase-space term, and it is given by [22, 26, 31]:

$$\frac{d^3\sigma}{d\Omega_\alpha d\Omega_{^7Be} dE_\alpha} \propto KF \cdot \phi(p_n)^2 \cdot \left(\frac{d\sigma}{d\Omega}\right)^{HOES}_{^{10}\mathrm{B+p}\rightarrow\alpha_0+^7\mathrm{Be}} \quad (1)$$

where

i: KF is a kinematical factor containing the final-state phase-space factor and it is a function of the masses, momenta, and angles of the outgoing particles [22, 26, 32];

ii: $\phi(p_n)^2$ is the squared Fourier transform of the radial wave function $\chi(\vec{r}_{p_n})$ describing the $p-n$ intercluster motion, given by the Hultheń function. Since the $p-n$ relative motion essentially takes place in s-wave, the momentum distribution has a maximum at $p_n = 0$. The contribution of the d-wave has been demonstrated to be negligible [33];

iii: $\left(\frac{d\sigma}{d\Omega}\right)^{HOES}_{^{10}\mathrm{B+p}\rightarrow\alpha_0+^7\mathrm{Be}}$ is the half-off-energy-shell (HOES) differential cross section of the ^{10}B(p,α_0)^{7}Be reaction at the center-of-mass energy E_{cm}, given in post-collision prescription (PCP) by the relation [34]:

$$E_{cm} = E_{\alpha-^7Be} - Q_{2b}, \quad (2)$$

where Q_{2b} is the Q-value of the ^{10}B(p,α_0)^{7}Be reaction and $E_{\alpha-^7Be}$ is the α-^{7}Be relative energy.

A proportionality sign is present owing to the use of the plane wave approximation, thus the two body-cross section that we can obtain is in arbitrary units [26], even if recent developments could make it possible to derive the binary cross section in absolute units [22].

B. From QF reactions to the THM

As it is apparent from the previous section, the THM is rooted in the theory of direct reaction mechanisms (see, e.g., [35, 36]) and in particular in the studies of the QF reaction mechanism (see [27] and references therein). The THM can be regarded as an extension to the ultra-low energies of QF reactions, making it possible to apply the method to nuclear astrophysics [21, 34, 37]. The methodology behind the THM application has been described in different articles [16, 26, 31, 38]. In the following paragraphs, we shortly summarize the main features, with particular reference to the ^{2}H(^{10}B,$\alpha_0{}^7$Be)n case.

1. Energy and Momentum Prescriptions

In the ^{2}H(^{10}B,$\alpha_0{}^7$Be)n measurement, the 27 MeV bombarding energy was chosen to overcome the ^{2}H-^{10}B Coulomb barrier (1.6 MeV). Thus, p is brought inside the nuclear interaction zone to induce the ^{10}B+$p\rightarrow\alpha_0+^7$Be reaction. Moreover, electron screening is a fortiori bypassed, since the distance of closest approach is significantly smaller than the atomic radius [39]. Yet, astrophysical energies can be reached since the projectile energy is compensated for by the binding energy of deuteron ([22, 26, 40] and references therein); in QF condition the interaction energy is:

$$E_{QF} = E_{p-^{10}B} - B_{pn}, \quad (3)$$

$E_{p-^{10}B}$ being the projectile energy in the ^{10}B-p center-of-mass system and B_{pn} the deuteron binding energy. Regarding momentum prescriptions, we need to select the neutron momenta for which the cross section can be essentially described by the single diagram in Fig.1 [22, 30]. This is accomplished by selecting only events with small p_n inter-cluster momenta, satisfying the condition [29, 30]

$$|\vec{p}_n| \leq |\vec{k}_n| \quad (4)$$

with $k_n = \sqrt{2\mu_{pn}B_{pn}}$, μ_{np} the $p-n$ reduced mass and B_{pn} the deuteron binding energy. For deuterons, this limit is $p_n \leq$44 MeV/c. Within this interval, deviations from the Hultheń function are negligible. (see for instance [29, 41, 42]). Beyond this interval, deviations from the pure Hulthén function start to be dominant, signalling that a PWIA description of the reaction mechanism is not realistic. In these cases, deviations can be evaluated via devoted computer codes, such as FRESCO [43].

2. Selection of the "Trojan Horse" Nucleus

In the THM approach, a so-called "Trojan Horse" (TH) nucleus is used to transfer the participant particle, a proton in the case of the ^{10}B(p,α_0)^{7}Be reaction. In the ^{2}H(^{10}B,$\alpha_0{}^7$Be)n measurement, a deuteron is used to supply virtual protons owing to its obvious $p \oplus n$ structure, its well known binding energy and internal wave function, and because the residual spectator particle is not charged, reducing the chances of distortions induced by the long-range Coulomb interaction. These make deuteron the best choice, in comparison with other systems that can be used to transfer protons, such as ^{3}He.

At present, all TH nuclei (^{2}H, ^{6}Li, ^{3}He, ^{14}N and ^{20}Ne) used to perform TH experiments, are characterized by an $l = 0$ orbital angular momentum for the intercluster motion. Thus, the momentum distribution of spectator nucleus (in this case the neutron) has a maximum for $|\vec{p}_s| = 0$. This choice is linked not only to the reduction of experimental difficulties when selecting the QF mechanism but also to theoretical considerations for the applicability of the pole approximation [30].

The extension to measurements with TH nuclei having $l = 1$ is desirable as it would allow for the investigation

TABLE I. Laboratory central angles (θ_0), covered angular ranges ($\Delta\theta$), solid angles ($\Delta\Omega$), distances from the target (d), thickness (s), effective area, and intrinsic angular resolution ($\delta\theta$) for each detector.

Detector	θ_0	$\Delta\theta$	$\Delta\Omega$	d	s	Area	$\delta\theta$
	(deg)	(deg)	(msr)	(mm)	(μ m)	(cm^2)	(deg)
PSD-1	16^o	$\pm 8^o$	1.5±0.1	167±2	1000	5	0.1
PSD-2	14^o	$\pm 6^o$	4.1±.4	195±2	500	5	0.1-0.2

FIG. 2. (Color online) Schematic drawing of the adopted experimental setup, showing the ΔE−E system, made up of a proportional counter (ΔE) and a position sensitive detector (PSD_2), devoted to ^{7}Be detection, and a position sensitive detector (PSD_1), optimized for alpha particle detection.

of nuclear reactions induced by virtual ^{3}H and ^{3}He, obtained from the cluster systems ^{7}Li = t+α and ^{7}Be = α+^{3}He, respectively.

III. THE EXPERIMENT

A. Experimental set-up

The ^{2}H(^{10}B,α^7Be)n experiment was performed at the Pelletron-Linac laboratory (Departamento de Fisica Nuclear (DFN)) in São Paolo (Brazil). The Tandem Van de Graaff accelerator provided the 27 MeV ^{10}B beam with a spot size on target of about 2 mm and intensities up to 1 nA. The relative beam energy spread $\Delta E_{beam}/E_{beam}$ was about 10^{-4}. The beam energy was chosen in order to span a ^{7}Be-p relative energy ranging from 1.5 MeV down to zero. This has been needed in order to investigate, under QF conditions, both the Gamow energy region of interest for astrophysics (i.e. E_G= 10±5 keV) as well as a higher energy region needed for normalization purposes. Additionally, the wide energy range allows us also to investigate possible interference effects between the resonances intervening in the ^{10}B(p,α_0)^{7}Be reaction as recently addressed in the work of [12, 13]. A self-supported deuterated polyethylene target (CD_2) of about 200 μg/cm^2 was placed at 90° with respect to the beam axis. The detection setup (Fig.2) consisted of a 1000 μm Position Sensitive Silicon Detector (PSD_1) and a telescope system, having a proportional counter (PC) as ΔE and a standard 500 μm PSD (PSD_2) as E detector. The PSD_1 detector was devoted to α detection and was placed at a distance d_1=167 mm from the target, covering the angular range 8°− 24°. The telescope devoted to ^{7}Be detection was placed at opposite side with respect to the beam direction, at a distance d_2=195 mm from the target, covering the angular ranges 8° − 20° (see Tab.I for details about the experimental setup).

The PC was filled with 13.3 mbar butane gas and a foil of 1.5 μm mylar was used as a window. The pressure of the gas inside the PC was monitored during the whole experiment through a standard pressure sensor. The experimental setup was chosen to cover the QF angular range, as given from kinematic simulations. An anti-scattering system was used to preserve detectors at small angles from scattered beam. Energy and position signals were processed by standard electronics and sent to the acquisition system for the on-line monitoring and data storage.

B. Angular and energy calibrations

First runs of the experiment were dedicated to position and energy detector calibration. Calibrations were performed by using the ^{12}C(^{6}Li,α)^{14}N, ^{12}C(^{6}Li,^{6}Li)^{12}C and ^{197}Au(^{6}Li,^{6}Li)^{197}Au reactions induced at beam energies of 10 MeV and 16 MeV as well as a ^{241}Am α-source. To perform position calibration, a frame with 4 equally spaced wires was placed in front of each PSD and then kept during the whole experiment in order to assure a continuous monitoring of the fixed angular position even after calibration. An optical system was used to measure the central angle of each detector and the angle of each wire with respect to the beam direction. Since the geometry of these masks is known, a cross check of the measured position was performed to reduce the possible systematic errors on detection angles. Deterioration of CD_2 targets was continuously monitored by checking the ratio of the Z=4 particle yield to the charge collected in the Faraday cup at the end of the beam line. The overall procedure lead to an energy resolution better than 1% and a position resolution of 0.3°.

IV. DATA SELECTION

A. Identification of events of the ^{2}H+^{10}B→α_0+^{7}Be+n reaction

The first step in channel identification is the selection of Z=4 particles using the standard ΔE-E technique, while no identification was used for α particles on PSD_1.

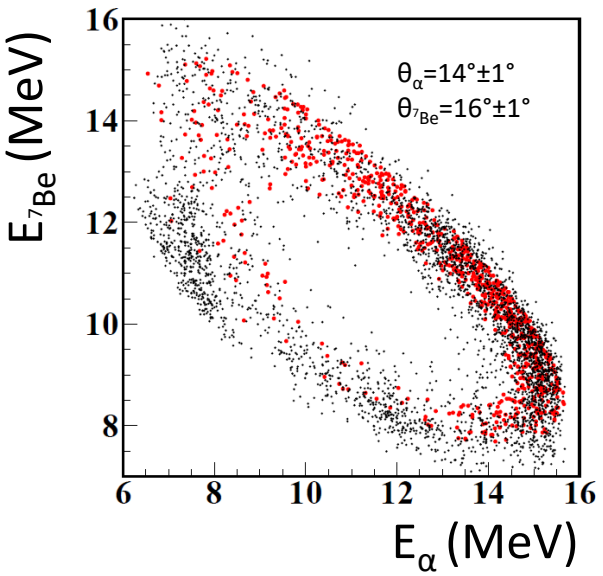

FIG. 3. (Color online) Experimental $E_{^7Be}$ vs. E_{α_0} kinematical locus at θ_{α_0}=14°±1° and $\theta_{^7Be}$=16°±1° (black dots), compared with the simulated locus, being detection thresholds and energy loss in the materials traversed by the detected particle fully accounted for (red circles).

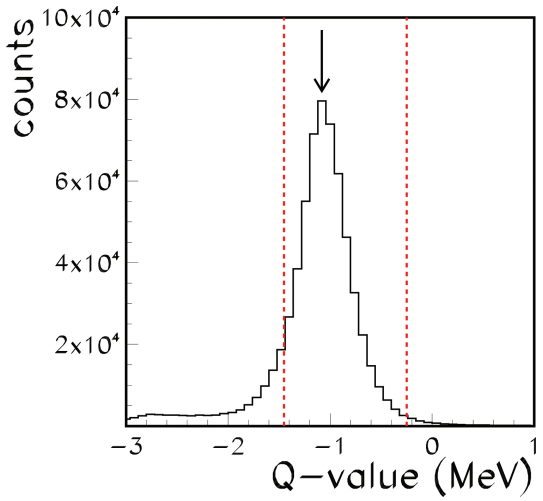

FIG. 4. (Color online)Experimental Q-value spectrum. The peak marked with the vertical arrow refers to the ^{2}H(^{10}B,α_0 ^{7}Be)n reaction. The vertical dashed lines mark the window on the Q-value adopted for the next stages of the data analysis.

Unfortunately, very poor energy resolution characterizes the PC, thus the Z=4 partly overlap with the peak arising from elastically scattered ^{10}B nuclei. Therefore, apart from the selection of the Z=4 locus, further checks are necessary to reject background events.

Since events from the ^{2}H+^{10}B→α_0+^{7}Be+n reaction gather along peculiar kinematic loci for each pair of detection angles, determined by energy and momentum conservation laws, the examination E_{PSD1} vs. E_{PSD2} plots for each pair of detection angles allows us to disentangle the target reaction from spurious events, assuming that the third undetected particle is a neutron. An example is given by Fig.3, where the chosen angular pair is θ_{PSD_1}=14°±1° and θ_{PSD_2}=16°±1° (similar results are retrieved for the other couples). Here, the energy detected in PSD_2 is reported in the vertical axis, while the energy deposited in PSD_1 is on the horizontal axis. Experimental data (black dots) clearly distribute along an ellipse, which can be attribute to events from the ^{2}H+^{10}B→α_0+^{7}Be+n reaction from the comparison with a simulated 2D spectrum (red dots), including all experimental effects such as energy loss in the dead layers and detection thresholds. Good agreement between the experimental and simulated kinematic loci is found for all the angular couples. The differences in the population of the kinematic loci is originated by reaction dynamics. Spurious events, due for instance to other competing reactions induced by the projectile and the CD_2 target, lie outside the picture area, thus they can be rejected by gating on the experimental kinematic plot. Such identification allows us to label the axes of Fig.3 with E_α and $E_{^7Be}$.

Assuming that the undetected particle is a neutron, as supported by the agreement between the experimental and simulated kinematic plots, we deduced the Q-value spectrum that is displayed in Fig.4. The theoretical Q-value is marked by an arrow in the figure (Q^{th}= -1.079 MeV). The Q-value spectrum shows a single peak at about Q^{exp}=-1.13±0.23 MeV, in agreement with the theoretical value. In the further analysis only events in the range -1.45 MeV≤Q-value≤-0.25 MeV are considered. In this way, additional background sources are removed. The measured background on this energy range is lower than the 5%.

B. Selection of QF events

1. *Relative energy two-dimensional plots*

Since THM equations can be applied only to the QF yield to deduce the binary cross section of interest, the QF mechanism has to be identified and separated from different reaction mechanisms. Sequential decay (SD) is especially affecting QF data selection, and it has attracted particular attention in the past years (see, for instance, [44, 45]). In detail, the ^{7}Be+α+n exit channel can be populated through three different paths, corresponding to the different couplings of n, ^{4}He and ^{7}Be:

1. ^{10}B+^{2}H→^{11}C*+n→^{7}Be+α+n
2. ^{10}B+^{2}H→^{8}Be*+α→^{7}Be+n+α
3. ^{10}B+^{2}H→^{5}He*+^{7}Be→α+n+^{7}Be

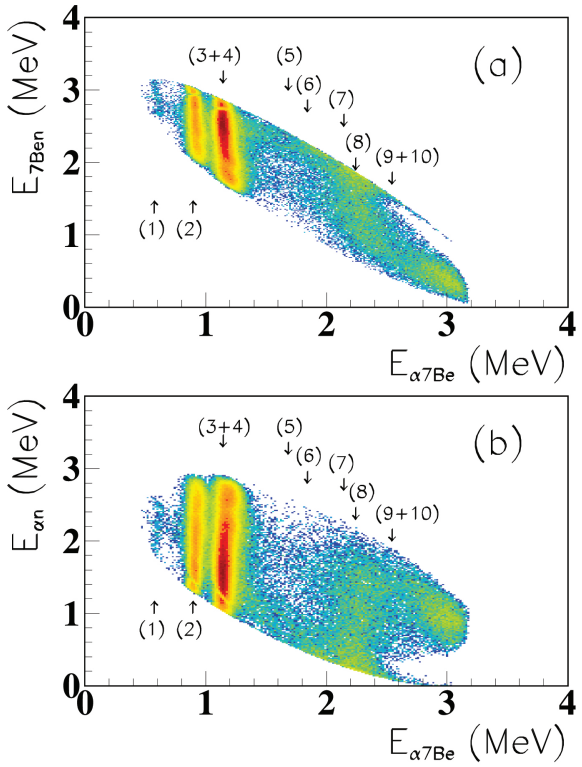

FIG. 5. (Color online) Relative energy scatter plots: (a) $E_{^7Be-n}$ *vs* $E_{\alpha-^7Be}$ (lower panel) and (b) $E_{\alpha-n}$ *vs* $E_{\alpha-^7Be}$ (upper panel). The arrows mark ^{11}C states discussed in the text.

Kinematic conditions can be chosen to minimize SD contributions in most cases; in particular, this is possible in a region of the three-body phase space where the neutron momentum (p_n) is small, i.e. where the neutron energy E_n is almost vanishing. We first focus on the SD processes taking place through the feeding of ^{8}Be* (case 2) and ^{5}He* (case 3). Under these circumstances, it is possible to identify contributions coming from SD by means of the analysis of the relative energy spectra for any pair of detected particles.

Fig. 5 shows the scatter plots of ^{7}Be-n and α-n relative energies as a function of the α-^{7}Be relative energy (upper and lower panels, respectively). In these plots, any event correlation appearing as an horizontal line gives evidence of the formation of ^{8}Be and ^{5}He excited intermediate system, respectively, finally feeding the exit channel of interest. Fig. 5 shows no horizontal loci, making it clear that eventual contribution from SD is well below the statistical uncertainty. Conversely, Fig. 5 demonstrates very clear vertical loci corresponding to ^{11}C levels at excitation energies of 8.104 MeV (labelled as (1)), 8.420 MeV (labelled as (2)), 8.654 MeV and 8.699 MeV (unresolved levels labelled as (3)+(4)), and less clear ones above 1.5 MeV of α-^{7}Be relative energy, corresponding to levels at 9.2 MeV (labelled as (5), not clear in this representation), 9.36 MeV (labelled as (6)), 9.645 MeV and 9.780 MeV (wide vertical locus from unresolved levels, labelled as (7)+(8)), 9970 MeV (labelled as (9)) and 10.083 (labelled as (10)). Therefore, the ^{2}H(^{10}B,α_0^{7}Be)n reaction mainly proceeds through formation of an intermediate ^{11}C excited nucleus. In contrast with ^{5}He and ^{8}Be states, however, this can be populated through both SD and QF reaction mechanisms, thus a more thoroughly examination of the process leading to ^{11}C formation is mandatory. In particular, only the 8.699 MeV and 9.200 MeV ^{11}C excited states might contribute within the astrophysical energy region, being the low lying states at 8.654, 8.420, and 8.104 MeV below the ^{10}B+p decay threshold and those at 9.360 MeV, 9.645 MeV, 9.780 MeV, 9.970 MeV, 10.083 MeV, very far from the Gamow energy (E_G=10 keV).

2. *Data as function of the neutron momentum p_n*

Eq.1 entails that a necessary condition for the occurrence of the QF mechanism is that the coincidence yield is proportional to the $p-n$ momentum distribution $\phi(p_n)^2$. However, the strong energy dependence of the differential cross section (at odds with angular dependence, since angular distributions are isotropic at low energies) and phase space effects conceal such dependence.

To validate our hypothesis, that is mandatory to proceed with the extraction of the astrophysical factor, we have selected the events corresponding to a very narrow window in $E_{^7Be-\alpha}$, 100 keV wide, right in correspondence of the (3)+(4) ^{11}C states, to lessen the influence of the $(d\sigma/d\Omega)^{HOES}$ factor, and projected onto the p_n axis. By correcting for the kinematical factor to remove phase-space effects, a quantity that is proportional to the momentum distribution should be obtained, the ^{10}B(p,α)^{7}Be two-body cross section being constant in the restricted relative energy chosen.

The resulting experimental momentum distribution $\phi(p_n)^2_{exp}$ is given as black circles in Fig.6. The vertical error bars include only statistical errors, while the horizontal bars mark the width of the data bins. The black solid line represents the theoretical distribution, namely, the squared Hulthén wave function in momentum space:

$$\phi(p_n)^2 = \frac{1}{\pi}\sqrt{\frac{ab(a+b)}{(a-b)^2}}\left[\frac{1}{a^2+{p_n}^2}-\frac{1}{b^2+p_n^2}\right] \qquad (5)$$

with parameters a= 0.2317 fm^{-1} and b=1.202 fm^{-1} [34]. This theoretical distribution was superimposed on the data, after being normalized to the experimental maximum, and reproduces quite well the shape of experimental data.

The red line superimposed onto the data represents the fit with the Hulthén function leaving b as free parameter. The best fit is obtained with b=0.81±0.49 fm^{-1}, corresponding to a reduced χ^2 of 0.2. By using b as a fitting parameter, the FWHM of the momentum distribution can be adjusted to the experimental one, to check

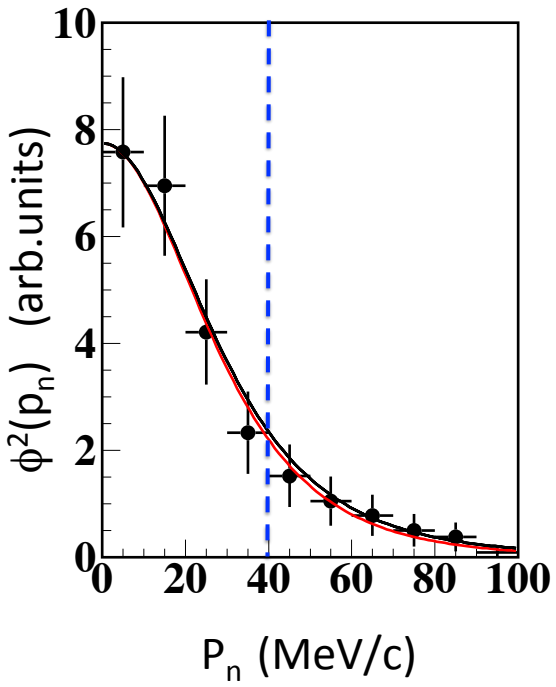

FIG. 6. (Color on line) Experimental momentum distribution (black circles) compared with the theoretical one (black line) given by the squared Hulthén wave function in momentum space. The red line represents the fit of the data with the Hulthén function leaving b as free parameter. The vertical error bars include only the statistical error, the horizontal ones the data bin width. The vertical line fixes the momentum region ($0 \leq p_n \leq 40$) MeV/c selected for the further analysis.

whether distortions induced, for instance, by rescattering between the particles in the final state might be relevant [29]. The experimental FWHM obtained in this way is 57±4 MeV/c, in very good agreement with the theoretical one FWHM_{th} = 58 MeV/c obtained under pure PWIA.

The agreement between the experimental and theoretical distributions shows that the dominant reaction mechanisms is the QF one and other reaction mechanisms, such as sequential decay, produce a contribution smaller than the statistical uncertainty, deviations from the Hulthén wave function in momentum space being not appreciable. Even if the agreement is good also at p_n values as large as 100 MeV/c, yet we have introduced a $p_n < 40$ MeV/c cut in the data to comply with Eq. 4, making any sequential decay contribution smaller a fortiori.

3. *Discussion on the FWHM of $\phi(p_n)^2$ momentum distribution vs. the momentum transfer q_t*

To check for departures from the simple PWIA, the measured FWHM value (57±4 MeV/c) and momentum

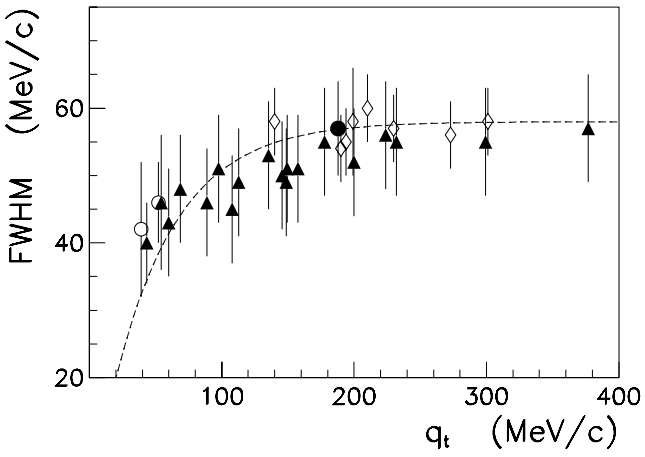

FIG. 7. FWHM for the n momentum distribution inside the deuteron as a function of the momentum transfer q_t (see [41, 42, 46]). The black dashed line represents Eq.6, whose free parameters have been fixed from a fit to experimental data shown as black triangles, open circles and open diamonds (see [41, 42] for a detailed description). The black circle is used to indicate the FWHM value obtained in this work, with the corresponding q_t value from the present experiment.

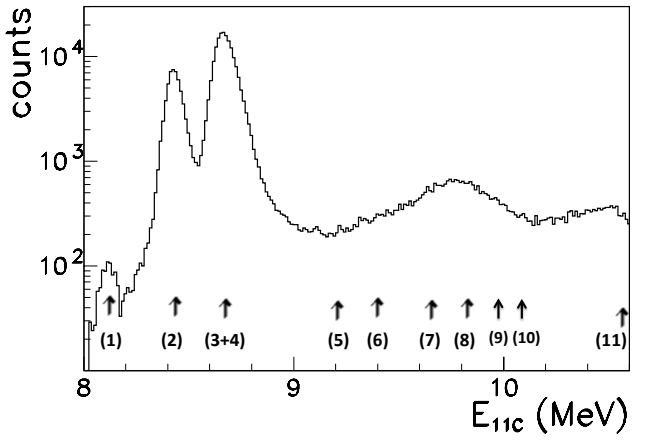

FIG. 8. (Events corresponding to the kinematical condition $p_n \leq 40$ MeV/c (as discussed in the text) projected onto the ^{11}C excitation energy axis. Labels and arrows highlight the position of known excited states of ^{11}C. The numbering is the same as in the previous figures.

transfer (q_t = 188 MeV/c) have been compared with the expected values based on the discussion reported in in [41, 42, 46]. In the PWIA framework, the dependence of the FWHM on q_t is given by:

$$W(q) = f_0[1 - \exp(-q_t/q_0)] \qquad (6)$$

with parameters f_0=58 MeV/c and q_0=48±2 MeV/c, obtained by fitting experimental data from literature as reported in [41, 42]. Its behaviour is shown in Fig.7 as a dashed line superimposed onto the experimental data sets (open circles and diamonds, solid triangles) used to fix the f_0 and q_0 parameters. The black solid circle refers to the measured FWHM and q_t values from this work. At q_t=188 MeV/c the theoretical curve gives a FWHM value of 56.5 MeV/c, in very good agreement within experimental errors with the present one. This result is an indication of negligible distortions and makes us confident of the use of PWIA approximation.

In conclusion of this section:

(i) in the experimentally selected kinematic regions, the QF mechanism gives the main contribution to the ^{10}B+d reaction at 27 MeV;

(ii) the QF mechanism is selected, without significant contribution from contaminant SD processes;

(iii) PWIA can be used to describe the process.

Further data analysis will be limited to events in the momentum region $|\vec{p}_n|\leq$40MeV/c, inside the theoretical limit given by Eq. 4 of section IIB.

V. ANALYSIS OF THE $E_{^{11}C}$ EXCITATION ENERGY SPECTRA

The coincidence yield of the $^{10}B + d \rightarrow {}^{7}Be + \alpha + n$ reaction, corresponding to the $p_n\leq$40 MeV/c momentum range, is shown in Fig.8 as a function of ^{11}C excitation energy. Two well separated peaks show up at 8104 keV (level (1)) and 8420 keV (level (2)), while the label (3+4) refers to the convolution of the 8654 keV (3) and the 8699 keV (4) levels. Labels (5) to (10) and corresponding arrows locate the positions of higher lying states not resolved in the figure and whose energies and resonance parameters are reported in Tab.II.

The experimental energy resolution has been evaluated by fitting the isolated 8.420 MeV level (label (2) of Fig.8) with a Gaussian function, since this level shows a very narrow natural width $\Gamma\sim 8\cdot 10^{-3}$ keV (see Tab.II). The data fit yields a FWHM equal to 87±5 keV, representing the energy resolution achieved in this work. The fit also gives a resonance energy E_R =8432±2 keV, to be compared with the one in the literature (see Tab.II), so a negligible energy shift of 12 keV is obtained, in comparison with the experimental energy resolution. The result of the fit is shown in Fig.9.

Fig.8 demonstrates that the 8.654 MeV and 8.699 MeV ^{11}C excited states (3+4) are not resolved owing to the experimental energy resolution (87 keV). Unfortunately, the 8.699 MeV state sits right at the Gamow peak energy for the the ^{10}B(p,α)^{7}Be reaction, making it necessary to disentangle the two contributions and to subtract from the experimental data the sub threshold state at 8.654 MeV. We apply the same procedure as in [16].

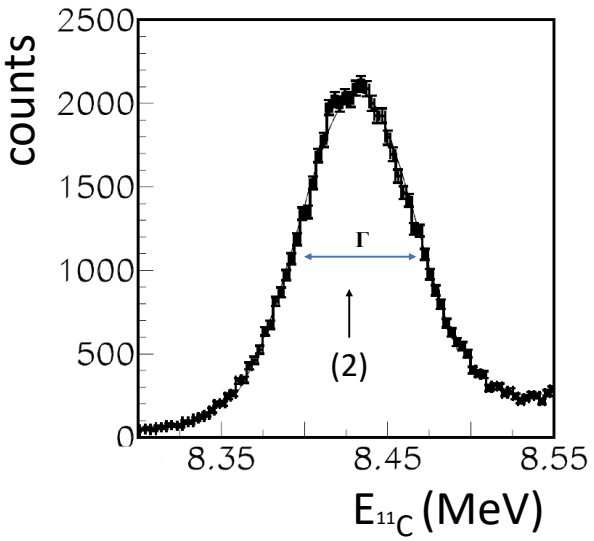

FIG. 9. Fit of the 8.420 MeV ^{11}C level with a Gaussian function to deduce the experimental energy resolution.

TABLE II. Resonance labels, resonance energies of the ^{11}C states populated in this work, corresponding E_{cm} values in the ^{10}B−p system, spin-parities, natural widths Γ_{cm} from the literature, observed decays and related references.

Level number	$E^*_{^{11}C}$ (MeV)	E_{cm} (keV)	J^π	Γ_{cm} (keV)	decay	Ref.
(1)	8.104±1.7	-585	$3/2^-$	$6^{+12}_{-2}\cdot 10^{-3}$	(γ,α)	[25]
(2)	8.420±2	-269	$5/2^-$	$8\cdot 10^{-3}$(fs)	(γ,α)	[25]
(3)	8.654±4	-35	$7/2^+$	≤5	(γ)	[25]
(4)	8.699±50	10	$5/2^+$	15±1	(γ,p)	[9]
(5)	9.200±50	511	$5/2^+$	500±90	(γ,p)	[25]
(6)	9.36±50	671	$(5/2^-)$	239	(p,α)	[12]
(7)	9.645±50	956	$(3/2^-)$	210±40	(γ,p,α)	[9]
(8)	9.780±50	1091	$(5/2^-)$	240±50	(γ,p)	[25]
(9)	9.970±50	1281	$(7/2^-)$	120±20	(γ,p)	[25]
(10)	10.083±5	1394	$7/2^+$	∼230	(γ,p,α)	[25]

The observed peak corresponding to the two unresolved levels (3)+(4) has been fitted by considering the broadening due to the energy resolution. The fitting function is expressed in terms of the incoherent sum of two Breit-Wigner shapes $bw(E)_{(3)}$, $bw(E)_{(4)}$, plus an additional term describing the contribution of the tail of the resonant level at 9.2 MeV, $bw(E)_{(5)}$, and a non resonant term $p(E)$:

$$F(E)_{unres.} = bw(E)_{(3)}+bw(E)_{(4)}+bw(E)_{(5)}+p(E) \quad (7)$$

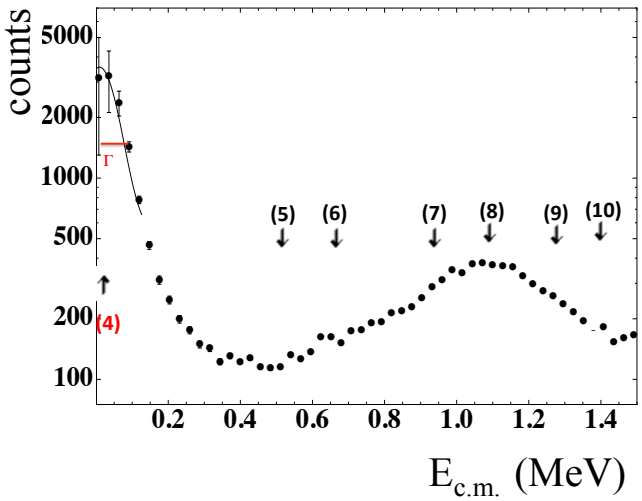

FIG. 10. $^{10}\mathrm{B}-p$ relative energy spectrum obtained by subtraction of the 8.654 MeV ^{11}C state and for $p_n < 40$ MeV/c.

with

$$bw(E)_{(i)} = N(E_{R_{(i)}}) \cdot \frac{\left(\frac{\Gamma_{(i)}}{2}\right)^2}{\left(E - E_{R_{(i)}}\right)^2 + \left(\frac{\Gamma_{(i)}}{2}\right)^2} \qquad (8)$$

and

$$p(E) = p_0 + p_1 E + p_2 E^2 + p_3 E^3. \qquad (9)$$

In the fitting, the resonance energies where fixed to the values of Tab.II, while the widths were calculated from the sum of the squared intrinsic widths of Tab.II and the energy resolution. The fitting procedure has yielded the following normalization parameters $N(E_{R_3})$=88000±300, $N(E_{R_4})$=12000±105, $N(E_{R_5})$=160±13 and the following coefficients for the non resonant term: $p_0 = 500$, $p_1 = -1308$ MeV^{-1}, $p_2 = 4775$ MeV^{-2} and $p_3 = -20000$ MeV^{-3}. The non resonant contribution $p(E)$ can be due to the direct breakup and/or to the tails of higher energy resonances (labels (6) and (7)), but no definitive conclusion can be drawn about its origin, as mentioned in [16]. However, this does not affect significantly the fitting procedure.

Using Eq.7, setting to zero the contribution of resonance (4) and of the non resonant part, it has been possible to subtract the contribution of the sub threshold resonance at 8.654 MeV [16]. The deduced coincidence yield is shown in Fig.10 as a function of the p-^{10}B relative energy E$_{c.m.}$.

The maximum of uncertainty $(\epsilon_{lev.sub.})_i$ coming from subtraction of the sub-threshold 8.654 MeV level, has been evaluated as

$$(\epsilon_{lev.sub.})_i = \frac{N_{ev}(E_i)^{[(3)+(4)]} - N_{ev}(E_i)^{(3)}}{N_{ev}(E_i)^{[(3)+(4)]}} \qquad (10)$$

where $N_{ev}(E_i)^{[(3)+(4)]}$ and $N_{ev}(E_i)^{(3)}$ are the number of events corresponding to the value of $F(E_i)_{unres.}$ and to $bw(E_i)_{(3)}$ at the energy E_i, respectively. Events thus selected, with the corresponding error bar, enter the extraction of the $^{10}\mathrm{B}(p,\alpha)^7\mathrm{Be}$ cross section.

VI. EXTRACTION OF THE $^{10}\mathrm{B}(p,\alpha)^7\mathrm{BE}$ ASTROPHYSICAL FACTOR

A. From the HOES to the OES cross section

Following the PWIA, the $^{10}\mathrm{B}+p \rightarrow \alpha+^7\mathrm{Be}$ differential cross section $\left(\frac{d\sigma(E)}{d\Omega}\right)^{HOES}$ is extracted by inverting Eq.1:

$$\left(\frac{d\sigma(E)}{d\Omega}\right)^{HOES} \propto \frac{d^3\sigma}{d\Omega_\alpha d\Omega_{^7Be} dE_\alpha} \cdot (KF \cdot \phi(p_n)^2_{exp.})^{-1} \qquad (11)$$

As already discussed, KF is calculated from masses, angles and momenta of the detected ^{7}Be and α particles and $\phi(p_n)^2_{exp}$ is given by the fit described in the text (red line in Fig.6). It has been proved that the HOES cross section is essentially linked to the OES one by the penetration factor of the Coulomb barrier [47–50], calculated introducing the correct wave number and interaction radius for the p-^{10}B system. The THM cross section is then obtained through the relation:

$$\left[\frac{d\sigma(E)}{d\Omega}\right]^{TH} = \left[\frac{d\sigma(E)}{d\Omega}\right]^{HOES} \cdot P_0(kR) \qquad (12)$$

with $\mathrm{P}_0(kR)$ the penetrability of the Coulomb barrier, for l=0 given by:

$$P_0(kR) = \frac{kr}{F_0^2(kR) + G_0^2(kR)} \qquad (13)$$

with F_0 and G_0 regular and irregular Coulomb functions for $l = 0$, and k and R the wave number and the interaction radius for the p-^{10}B system, respectively. Here, the s-wave only is considered as it is dominant at such low energies [10]. In fact, the angular distributions for the $^{10}\mathrm{B}(p,\alpha_0)^7\mathrm{Be}$ reaction are essentially isotropic in the whole energy region explored here [10, 12]. Since the angular distributions are isotropic, they can be easily integrated over the entire solid angle to obtain the total cross section, which is expressed in arbitrary units since PWIA is used.

B. Calculation of $S_b(E)$-factor

To remove the strong energy dependence due to the Coulomb penetration, the astrophysical $S(E)$ factor is introduced via the relation:

$$S_b(E) = E\sigma_b(E)exp(2\pi\eta) \qquad (14)$$

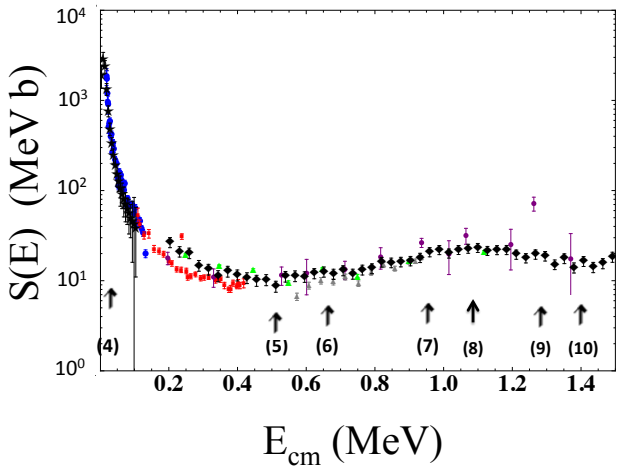

FIG. 11. (Color on line) Comparison of the THM bare-nucleus S-factor with the data in the literature. Present-work data are shown as solid diamonds, while red symbols mark the direct data from [10], corrected for the factor 1.83 as recommended in [18], blue symbols the data from [18], and purple symbols the thick-target data in [8]. Green and grey triangles are used for the recent works [13] and [12], respectively. The numbered arrows mark the ^{11}C states contributing, as listed in Table II.

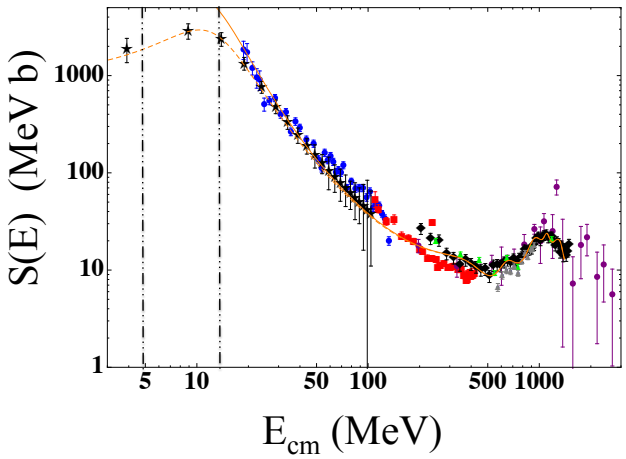

FIG. 12. (Color on line) R-matrix fit (dashed line) of the THM data from the present work above 200 keV and of the data of [16]. The present-work THM $S(E)$ factor in absolute units is displayed as black diamonds, while the data from [16] are shown as black stars. Red symbols mark the direct data from [10], corrected for the factor 1.83 as recommended in [18], blue symbols the data from [18], and purple symbols the thick-target data in [8]. Green and grey triangles are used for the recent works [13] and [12], respectively. The screened S-factor (with $U_e = 410$ eV) is shown as a full line.

where E is the energy in the center of mass system, η is the Sommerfeld parameter

$$\eta = \frac{Z_1 Z_2 e^2}{\hbar v} \tag{15}$$

where Z_1 and Z_2 represent the charges of interacting nuclei, v is their relative velocity and $exp(2\pi\eta)$ is the reciprocal of the Gamow factor.

Introducing the integrated THM cross section, the bare nucleus astrophysical $S_b(E)$-factor in arbitrary units is obtained. We use the subscript "b" to emphasize that the astrophysical factor obtained using the THM is devoid of electron screening enhancement, at odds with the direct one.

C. Normalization of the THM $S_b(E)$ factor

The THM astrophysical factor in absolute units has been obtained by normalization to direct data from [8, 12, 13]. In detail, we have fitted a scaling factor N multiplying the THM S$_b$-factor to the direct data, weighed by their uncertainties, over the $0.2 - 1.2$ MeV energy interval. The procedure yielded a reduced χ^2 of 2.2, while the error affecting the normalization constant is 4%. This is the normalization error to be added to the other sources of uncertainty. Fig.11 shows the normalized THM S-factor (black diamonds) superposed on the direct data from [13] (green triangles), [12] (grey triangles), [8] (purple circles), [18] (blue circles), [10] (red squares), and with published THM data [16] (black stars). A very good agreement is found between the direct data (especially the data from [13]) and the THM ones after normalization. The error bars affecting the THM $S(E)$ factor include the statistical error, the uncertainty connected to the sub-threshold level subtraction, the uncertainty derived from the choice of the nuclear radius in the penetrability factor (R in Eq.13) and the uncertainty due to the normalization procedure. The THM S$_b$-factor obtained in the present work is reported in Tab.III

VII. R-MATRIX ANALYSIS OF THE THM DATA

An R-matrix fit of the THM data has been performed. In the calculation, since no new THM data are available below 200 keV, the fitting parameters of the lowest laying resonances at 10 keV and 500 keV were fixed to those in [16] (see Tab.III for the resonance parameters). This choice has been suggested by the occurrence of a very pronounced resonance at 10 keV, which dominates the astrophysical factor up to about 200 keV. Moreover, it turns out that the THM S-factor obtained in this work perfectly matches with this R-matrix calculation from [16] up to about 400 keV, corroborating the accuracy of both indirect data sets coming from two independent experiments and analysis. Above 400 keV, the presence of the resonances discussed for instance in [12] cannot

TABLE III. THM S_b-factor. In the columns, the ^{10}B-p relative energy, the THM astrophysical factor, the total uncertainty $\Delta S(E)$, statistical ϵ_{stat} and total ϵ_{tot} errors (in percent) are given.

E_{cm} (keV)	$S(E)$ (MeV b)	ΔS(E) (MeV b)	$\epsilon_{stat.}$ %	$\epsilon_{tot.}$ %	E_{cm} (keV)	$S(E)$ (MeV b)	ΔS(E) (MeV b)	$\epsilon_{stat.}$ %	$\epsilon_{tot.}$ %
203.5	26.7	1.5	3.5	5.7	875.5	16.2	0.9	3.2	5.5
231.5	21.1	1.2	3.7	5.8	903.5	16.6	0.9	3.0	5.4
259.5	20.3	1.2	3.6	6.0	931.5	18	1	2.8	5.3
287.5	14.7	0.9	4.2	6.1	959.5	20.8	1.2	2.8	5.3
315.5	13.4	0.8	4.4	6.2	987.5	22	1	2.7	5.2
343.5	11.3	0.7	4.4	6.3	1015.5	20.1	1.1	2.6	5.2
371.5	12.7	0.8	4.5	6.3	1043.5	22	1.2	2.5	5.1
399.5	11.6	0.7	4.4	6.3	1071.5	22.7	1.2	2.5	5.2
427.5	10.7	0.7	4.5	6.4	1099.5	23.2	1.2	2.6	5.2
455.5	10.1	0.6	4.6	6.5	1127.5	21.5	1.1	2.6	5.1
483.5	10.2	0.6	4.4	6.5	1155.5	22	1.2	2.7	5.2
511.5	8.7	0.5	4.3	6.2	1183.5	22	1.2	2.9	5.3
539.5	11.1	0.5	4.4	6,2	1215.5	19.6	1.1	3	5.4
567.5	11.3	0.7	4.3	6.2	1239.5	17.8	1	3.1	5.5
595.5	11.1	0.7	4.1	6.1	1267.5	19.6	1.1	3.2	5.5
623.5	12	0.7	3.9	5.9	1295.5	18.8	1	3.3	5.6
651.5	12.6	0.7	4.0	0.6	1323.5	15.1	0.9	3.6	5.7
679.5	11.8	0.7	3.8	5.9	1351.5	17.7	1	3.7	5.8
707.5	13.	0.7	3.7	5.8	1379.5	13.9	0.8	3.8	5.8
735.5	12	0.7	3.7	5.8	1407.5	16.4	1	3.9	5.9
763.5	13.2	0.8	3.6	5.8	1435.5	14.1	0.8	4	6
791.5	13.7	0.9	3.7	5.7	1463.5	15.6	0.9	4	6
819.5	16.1	0.9	3.3	5.6	1491.5	18.3	1	4	6
847.5	15.9	0.9	3.2	5.5					

be neglected and urged us to perform a new R-matrix analysis of the THM data. In the fitting, besides the resonances at 10 keV and 500 keV that were not fitted, we introduced the same levels considered in the extensive R-matrix fitting performed in [12], using the fitting parameters there obtained as starting values of the R-matrix fitting of THM data. The THM measurement was focused only on the α_0 channel, namely on those events where the emitted α particle leaves the residual ^{7}Be nucleus in its ground state. Therefore, in the THM analysis the parameters for the α_1 channel were fixed to those of [12]. Regarding the 10.10 MeV ^{11}C state, that play a minor role, its presence seems to be not necessary for a satisfactory reproduction of THM data.

Fig.12 shows the resulting R-matrix fit (dashed line), superposed on the present-work $S(E)$ factor in absolute units displayed as black diamonds, and with the previous data sets: Ref.[16] S-factor shown as black stars, Ref.[10] data, corrected for the factor 1.83 as recommended in [18], as red squares, Ref.[18] as blue circles, thick-target data in [8] as purple circles, and recent works [13] and [12] S-factors as green and grey triangles, respectively. The R-matrix fit nicely describes the astrophysical factor below about 1500 keV. The resonance parameters are collected in Tab.IV. Interestingly, this work confirms the occurrence of the 9.36 MeV ^{11}C state, in agreement with the results in [12] and in [13]. In general, there is very good agreement between the resonance parameters of Tab.IV and those in Tab. 1 of [12], but the 1.291 MeV resonance seems to be significantly narrower in our fit. This might be attributed to the introduction of a non resonant contribution in this work, which was not considered in [12]. Indeed, it is important noting that a non resonant contribution has been added in the fitting, by considering a very broad resonance at 30 MeV, leading to a non resonant term of about 3 MeVb, constant across the whole energy window discussed in this work. Finally, the enhancement at energies lower than 50 keV has been

TABLE IV. Resonance energies of the ^{11}C states populated included in the R-matrix fit, corresponding $E_{c.m.}$ values in the ^{10}B$-p$ system, spin-parities, Γ_p and Γ_{α_0} values. Resonance parameters below 600 keV are taken from [16], while Γ_{α_1} widths are taken from [12].

$E^*_{^{11}C}$ (MeV)	$E_{c.m.}$ (MeV)	J^π	Γ_p (keV)	Γ_{α_0} (keV)	Γ_{α_1} (keV)
9.36	0.671	$5/2^-$	4	235	< 0.1
9.65	0.961	$3/2^-$	48	223	< 0.1
9.80	1.111	$5/2^-$	12	116	4
9.98	1.291	$7/2^-$	221	30	4
10.02	1.331	$7/2^+$	13	105	1
10.67	1.981	$9/2^+$	126	37	< 0.1

described by using the electron screening potential value of 430 eV given in [11] (solid line).

1. New normalization of the low-energy S-factor

The concurrent availability of THM data up to about 1.5 MeV and of new improved direct measurements [12, 13] in the energy region where no electron screening is present, represents a very good opportunity to revise the THM low-energy S-factor, (7)), stretching down to the Gamow window, reported in [16]. Indeed, before the two measurements [12, 13] were published, only data affected by large uncertainties were available above about 100 keV, namely those in [10] probably affected by a systematic error in absolute normalization [11], and those in [8]. As discussed above, by performing a weighted scaling of the THM S-factor to the available direct data the normalization error turned out to equal 4%, which is significantly smaller than what given in [16], namely 18%. By using our R-matrix fitting, connecting the present data with those laying below 100 keV in [16], we were able to perform a new normalization of this data and calculate the corresponding normalization uncertainty. Clearly, the total uncertainties are much narrower than in [16] owing the improved normalization procedure. The renormalized low-energy S-factor and the total uncertainties are given in Tab.V.

Particular emphasis should be given to the bare-nucleus S-factor at zero energy ($S_b(0)$) and at 10 keV (S_b(10 keV)), corresponding to the Gamow peak energy. Using the new improved normalization we obtained $S_b(0)$ = 1192± 238 MeV b and S_b(10 keV) = 2942±398 MeV b, with the errors including statistical, subthreshold subtraction, channel radius, and normalization uncertainties. For ease of comparison, we collect the values of $S_b(0)$ and S_b(10 keV) deduced by means of different approaches (extrapolation and indirect measurements, for instance) in Tab.VI. Clearly, the present results, in agreement with the extrapolated value in [11], shows an improved accuracy as it is not an extrapolation but a real measurement right at astrophysical energies.

TABLE V. Unfolded experimental astrophysical $S(E)$ factor from [16] renormalized as discussed in the text. The columns contain the $p-^{10}$B relative energy, the bare nucleus astrophysical factor, the total error (including the effect of the change on the interaction radius R on the penetration factor $\sim 2\%$ and the normalization error 4%, besides the level subtraction error), the statistical error in percent, the level subtraction uncertainty in percent and the total error in percent.

E_{cm} (keV)	$S(E)$ (MeV b)	ΔS(E) (MeV b)	$\epsilon_{stat.}$ %.	$\epsilon_{lev.sub.}$ %	$\epsilon_{tot.}$ %
3.9	1995	394	9	17	20
8.9	3071	395	8	9	13
13.9	2530	277	8	6	11
18.9	1411	158	9	5	11
23.9	797	86	9	4	13
28.9	496	64	11	5	11
33.9	336	49	13	5	14
38.9	244	43	16	6	17
43.9	185	34	17	6	18
48.9	146	35	22	9	24
53.9	119	23	27	12	30
58.9	99	96	83	51.	97
63.9	84	76	78	46	90
68.9	72	28	36	14	90
73.9	63	51	73	37	82
78.9	56	22	38	12	31
83.9	49	23	44	15	47
88.9	44	26	56	21	60
93.9	40	39	90	38	98
98.9	36	44	100	71	100
103.9	33	23	65	22	69

2. Improved determination of the electron screening potential

Thanks to the reduced normalization error, a more accurate low-energy S-factor has been deduced below 100 keV, making it possible to improve the determination of the electron screening potential U_e, characterizing the exponential increase of S(E) owing to the presence of atomic electrons. Electron screening significantly alters the low-energy trend of the $S(E)$ factor, thus its effect has to be removed before astrophysical applications, being electron

TABLE VI. The bare nucleus ^{10}B(p,α)^{7}Be $S(E)$-factor at zero energy and at 10 keV obtained in the present work and from the literature

$S(0)$ (MeV b)	S(10 keV) (MeV b)	Approach	Ref.	Year
——	2200±600	Direct exp.	[10]	1991
——	2870±500	Direct exp.	[11]	1993
900	3480	DWBA	[17]	1996
1116±201	3105±559	R-matrix	[16]	2014
1192±298	2942±588	THM	[16]	2014
1116±45	3127 ±583	R-matrix	present work	2016
1192±238	2942±398	THM	present work	2016

TABLE VII. Electron screening potential for the boron+proton system. It is worth noting that in the ^{10}B-p direct measurement the same U$_e$ potential deduced from the ^{11}B-p measurement is adopted, while the THM measurement provides an independent U$_e$ determination for the boron+proton system starting from the p-^{10}B- reaction.

Reaction	U_e (eV)	Approach	reference	Year
^{11}B$(p,\alpha)^{8}$Be	430±80	Direct exp.	[11]	1993
	472±120	THM	[15]	2012
^{10}B$(p,\alpha)^{7}$Be	430±80	Direct exp.	[11]	1993
	240±200	THM	[16]	2014
	240±50	THM	present work	2016

screening in stellar plasmas very different from the one in the laboratory [3]. In the case of the direct measurements, extrapolation is necessary to determine the trend of the bare-nucleus S-factor, possibly leading to unpredictable systematic errors.

Since the THM allows us to measure the bare-nucleus astrophysical factor $S_b(E)$, namely, the one for fully stripped nuclei, it is possible to derive U_e from the comparison of $S_b(E)$ with the one deduced from direct measurements. This is done by fitting the available low-energy direct data of [11] by using the renormalized THM $S_b(E)$ factor [16] multiplied by the enhancement factor f_{lab} [3, 39, 51]:

$$S_s(E) = S_b(E)\ \exp\left(\pi\eta\frac{U_e}{E}\right), \qquad (16)$$

where U_e is left as the only free parameter in the best-fit procedure and the subscript "s" is used to underline that the S-factor from direct measurements is affected by the electron screening. This procedure yields $U_e = 240 \pm 50$ eV, clearly displaying a significant improvement in the uncertainty. For ease of comparison, the values of U_e available so far are collected in Tab.VII.

VIII. CONCLUSIONS

Triggered by the new ^{10}B$(p,\alpha)^{7}$Be astrophysical factors measured at energies above $\sim$ 200 keV [12, 13], and by the ambiguity affecting direct data in this energy interval, we have performed a new indirect measurement of the ^{10}B$(p,\alpha)^{7}$Be S-factor by applying the THM to the ^{10}B$(d,\alpha_0{}^{7}\mathrm{Be})n$ QF reaction. The QF reaction mechanism has been singled out by analyzing the relative energy spectra and extracting the experimental momentum distribution for the $p-n$ intercluster motion inside deuteron. The QF reaction yield is characterized by the population of many different resonant levels of the intermediate ^{11}C nucleus, though only the 8.699 MeV one is of primary importance for the ^{10}B$(p,\alpha)^{7}$Be $S(E)$ factor at astrophysical energies. In fact, the Gamow peak for typical boron quiescent burning is centered at 10 keV and coincides with the 8.699 MeV ^{11}C state. The extracted bare-nucleus S-factor turns out to be affected by a quite large energy resolution, 87 keV FWHM, which is well suited at higher energies, where comparatively broad resonances show up, but it is not good enough to explore the energy region below about 200 keV.

Therefore, the main aim of this work is to obtain a normalization to direct data [8, 12, 13] in a very large energy range (200-1200 keV) to reach a very low normalization uncertainty (4%). In this way we have obtained a significant improvement on the total error budget affecting the previous TH experiment, more focused on the low energy reaction, where the uncertainty on normalization was $\sim$18-20% [16]. The effect of the reduced normalization error influences both the 10 keV astrophysical factor, leading to a more accurate $S_b(10\,\mathrm{keV}) = 3127 \pm 583$ MeVb value, and the determination of the electron screening potential, 240±50 eV, where the quoted uncertainties include statistical, subthreshold level subtraction, normalization, and channel radius uncertainties.

In the light of this new improved results, it would be very interesting to perform a new measurement with improved energy resolution in the same energy interval, between 0.2 MeV and 1.5 MeV, and investigate also the energy beyond 1.5 MeV, the existing direct data being of rather poor quality. Moreover, it would be interesting to inspect the α_1 channel as well, corresponding to the decay of ^{11}C leaving ^{7}Be in its first excited state; in fact, even if this is of lesser importance, this channel would improve the understanding of ^{11}C spectroscopy [12]. Finally, the exam of the n+^{10}B channel would be of interest for the spectroscopy of the ^{11}B mirror nucleus, a channel that is present in our data as it is attributed to the neutron transfer off d. All these studies are presently ongoing, aiming at providing a full description of the ^{10}B$(p,\alpha)^{7}$Be

reaction at astrophysical energies.

ACKNOWLEDGMENTS

The authors are indebted to Prof. Teresa Borello for the help in setting up the experiment. This work has been partially supported by the Italian Ministry of University MIUR under the grant "LNS-Astrofisica Nucleare (fondi premiali)" and RFBR082838 (FIRB2008). The brazilians acknowledge the support from FAPESP and CNP_q. This work has been partially supported also by the grant LH1101 of the AMVIS project. A.M.M. also acknowledges the support by the US National Science Foundation under Award PHY-1415656.

[1] M. Freer, N. L. Achouri, C. Angulo, N. I. Ashwood, D. W. Bardayan, S. Brown, W. N. Catford, K. A. Chipps, N. Curtis, P. Demaret, C. Harlin, B. Laurent, J. D. Malcolm, M. Milin, T. Munoz-Britton, N. A. Orr, S. D. Pain, D. Price, R. Raabe, N. Soić, J. S. Thomas, C. Wheldon, G. Wilson, and V. A. Ziman, Phys. Rev. C **85**, 014304 (2012).

[2] H. Yamaguchi, D. Kahl, Y. Wakabayashi, S. Kubono, T. Hashimoto, S. Hayakawa, T. Kawabata, N. Iwasa, T. Teranishi, Y. K. Kwon, D. N. Binh, L. H. Khiem, and N. N. Duy, Phys. Rev. C **87**, 034303 (2013), arXiv:1212.5991 [nucl-ex].

[3] C.Rolfs and W.S.Rodney, *Cauldrons in the Cosmos* (The University of Chicago, 1988) p. 561.

[4] A.M.Boesgaard, C.P.Deliyannis, and A.Steinhauer, Astrophys. Journ. **621**, 991 (2005).

[5] R.J.Peterson et al., Ann. Phys. Energy **2**, 503 (1975).

[6] A.Kafkarkou, M.W.Ahmed, P.H.Chu, R.H.France, H.J.Karwowski, D.P.Kendellen, G.Laskaris, I.Mazumdar, J.M.Mueller, L.S.Myers, R.M.Prior, M.H.Sikora, M.C.Spraker, H.R.Weller, and W.R.Zimmerman, Nucl. Instrum. Method in Phys Res.B **316**, 015106 (2013).

[7] J.Szabo, J.Csikai, and M.Vaŕnagy, Nucl. Phys. **A195**, 527 (1972).

[8] N.A.Roughton, R.Fritts, R.J.Peterson, C.S.Zaidins, and C.J.Hansen, Nucl. Phys. **23**, 177 (1979).

[9] M.Wiescher, R.N.Boyd, S.L.Blatt, L.J.Rybarcyk, J.A.Spizuoco, R.E.Azuma, E.T.H.Clifford, J.D.King, J.Grres, C.Rolfs, and A.Vlieks, Phys. Rev. C **28**, 1431 (1983).

[10] M.Youn, H.T.Chung, J.C.Bhang, and K.-H.Chung, Nucl. Phys. A **533**, 321 (1991).

[11] C.Angulo, S.Engstler, G.Raimann, C.Rolfs, W.H.Schulte, and E.Somorjai, Z. Phys. A **345**, 231 (1993).

[12] I. Lombardo, D. Dell'Aquila, F. Conte, L. Francalanza, M. La Cognata, L. Lamia, R. La Torre, G. Spadaccini, C. Spitaleri, and M. Vigilante, J. Phys. G: Nucl. Part. Phys. **43**, 045109 (2016).

[13] A. Caciolli, R. Depalo, C. Broggini, M. La Cognata, L. Lamia, R. Menegazzo, L. Mou, S.M.R. Puglia, V. Rigato, S. Romano, C. R. Alvarez, M. Sergi, C. Spitaleri, and A. Tumino, The European Physics Journal A **52**, 136 (2016).

[14] L.Lamia, C.Spitaleri, N.Carlin, S. Cherubini, M. D. S. M.Gulino, M. La Cognata, M.G.Munhoz, R.G.Pizzone, S.M.R.Puglia, G.G.Rapisarda, S. Romano, M.L.Sergi, A.S.De Toledo, S.Tudisco, and A.Tumino, Il Nuovo Cimento C **31**, 423 (2008).

[15] L.Lamia, C.Spitaleri, V.Burjan, N.Carlin, S.Cherubini, V.Crucilla, M.G.Gameiro Munhoz, M.G.Gimenez Del Santo, M.Gulino, Z.Hons, G.G.Kiss, V.Kroha, S.Kubono, M.La Cognata, C.Li, J.Mrazek, A.Mukhamedzhanov, R.G.Pizzone, S.M.R.Puglia, Q.Wen, G.G.Rapisarda, C.Rolfs, S.Romano, M.L.Sergi, E.Somorjai, F.A.Souza, F. A., A.Szanto de Toledo, G.Tabacaru, A.Tumino, Y.Wakabayashi, H.Yamaguchi, and S.-H. Zhou, Journ. Phys. G **39**, 015106 (2012).

[16] C.Spitaleri, L.Lamia, S.M.R.Puglia, S.Romano, M.La Cognata, V.Crucilla, R.G.Pizzone, G.G.Rapisarda, M.L.Sergi, M.Gimenez Del Santo, N.Carlin, M.G.Munhoz, F.A.Souza, A.Szanto de Toledo, A.Tumino, B.Irgaziev, A.Mukhamedzhanov, G.Tabacaru, V.Burjan, V.Kroha, Z.Hons, J.Mrazek, Shu-Hua Zhou, C. Li, Q. Wen, Y.Wakabayashi, H.Yamaguchi, and E.Somorjai, Phys. Rev. C **90**, 035801 (2014).

[17] T.Rauscher and G.Raimann, Phys. Rev. C **53**, 2496 (1996).

[18] C.Angulo, M.Arnould, M.Rayet, P.Descouvemont, D.Baye, C.Leclercq-Willain, A.Coc, S.Barhoumi, P.Auger, C.Rolfs, R.Kunz, J.W.Hammer, A.Mayer, T.Paradellis, S.Kossionides, C.Chronidou, K.Spyrou, S.Degl'Innocenti, G.Fiorentini, B.Ricci, S.Zavatarelli, C.Providencia, H.Wolter, J.Soares, C.Grama, J.Rahighi, A.Shotter, and M.Lamehi-Rachti, Nucl. Phys. A **656**, 3 (1999).

[19] Y. Xu, K. Takahashi, S. Goriely, M. Arnould, M. Ohta, and H. Utsunomiya, Nucl. Phys. A **918**, 61 (2013).

[20] G.Baur, Phys.Lett. **178**, 135 (1986).

[21] C.Spitaleri, *Problems of Fundamental Modern Physics*, edited by R. Cherubini, P. Dalpiaz, and B. Minetti (World Scientific, New York, 1991) p. 211.

[22] R.E.Tribble, C.A.Bertulani, M.La Cognata, A.M.Mukhamedzhanov, and C.Spitaleri, Rep. Progr. Phys. **77**, 106901 (2014).

[23] A. M. Mukhamedzhanov, M. La Cognata, and V. Kroha, Phys. Rev. C **83**, 044604 (2011).

[24] G. Baur, C. Bertulani, and H. Rebel, Nucl. Phys. A **458**, 188 (1986).

[25] J. H. Kelley, E.Kwan, J.E.Purcell, C.G,Sheu, and H.R.Weller, Nucl. Phys.A **880**, 88 (2012).

[26] C.Spitaleri, A.M.Mukhamedzhanov, L.D.Blokhintsev, M.La Cognata, R.G.Pizzone, and A.Tumino, Physics of Atomic Nuclei **74**, 1763 (2011).

[27] C.Spitaleri, A.Tumino, M.Lattuada, R.G.Pizzone, S.Tudisco, D.Miljanic, S.Blagus, M.Milin, N.Skukan, and N.Soic, Phys. Rev. C **91**, 024612 (2015).

[28] I.S.Shapiro et al., Nucl. Phys. A **61**, 353 (1965).

[29] I.S.Shapiro, *Interaction of High-Energy Particles with Nuclei, International School of Physics "Enrico Fermi",*

Course 38, edited by E. Ericson (Academic Press, New York, 1967) p. 210.
[30] I.S.Shapiro, Sov. Physics Uspekhi **10**, 515 (1968).
[31] C.Spitaleri, *Interaction of High-Energy Particles with Nuclei, International School of Physics Enrico Fermi, Course*, edited by A.Bracco and E.Nappi (Academic Press, New York, 2011) p. 210.
[32] C.Spitaleri, A.Tumino, M.Lattuada, R.G.Pizzone, S.Tudisco, D.Miljanic, S.Blagus, M.Milin, N.Skukan, and N.Soic, The European Physics Journal **A 1**, 1 (2016).
[33] L. Lamia, M. La Cognata, C. Spitaleri, B. Irgaziev, and R. G. Pizzone, Phys. Rev. C **85**, 025805 (2012).
[34] M.Zadro, D.Miljanic, C.Spitaleri, Calvi, M.Lattuada, and F.Riggi, Phys. Rev. C. **40**, 181 (1989).
[35] G. R. Satchler, *Direct Nuclear Reactions, International Series of Monographs on Physics* (Oxford University Press, 1983) p. 211.
[36] C.A. Bertulani and P. Danielewicz, *Introduction to Nuclear Reactions* (IOP Publishing, London, 2004) p. 1.
[37] G.Calvi, M.Lattuada, D.Miljanic, F.Riggi, C.Spitaleri, and M.Zadro, Phys. Rev. C. **41**, 1848 (1990).
[38] C.Spitaleri, L.Lamia, A.Tumino, R.G.Pizzone, S.Cherubini, A.Del Zoppo, P.Figuera, M.La Cognata, A.Musumarra, M.G.Pellegriti, A.Rinollo, C.Rolfs, S.Romano, and S.Tudisco, Phys. Rev. C **69**, 055806 (2004).
[39] H.Assenbaum, K.L.Langanke, and C.Rolfs, Z. Phys. A **327**, 461 (1987).
[40] C.Spitaleri, M.Aliotta, S.Cherubini, M.Lattuada, D.Miljanic, S.Romano, N.Soic, M.Zadro, and R.A. Zappala, Phys. Rev. C **60**, 055802 (1999).
[41] R.G.Pizzone, C.Spitaleri, S.Cherubini, M.La Cognata, M.Lamia, D.Miljanic, A.Musumarra, S.Romano, A.Tumino, S.Tudisco, and S.Typel, Phys. Rev. C **71**, 055801 (2005).
[42] R.G.Pizzone, C. Spitaleri, A. M. Mukhamedzhanov, L. D. Blokhintsev, C. A. Bertulani, B. F. Irgaziev, M. La Cognata, L. Lamia, and S. Romanol, Phys. Rev. C **80**, 025807 (2009).
[43] I.J.Thompson, Comput. Phys. Rep. **7**, 167 (1987).
[44] M. La Cognata, S. Palmerini, C. Spitaleri, I. Indelicato, A. M. Mukhamedzhanov, I. Lombardo, and O. Trippella, Astrophys. J. **805**, 128 (2015).
[45] M. La Cognata, V. Z. Goldberg, A. M. Mukhamedzhanov, C. Spitaleri, and R. E. Tribble, Phys. Rev. C **80**, 012801 (2009).
[46] S.Barbarino, M.Lattuada, F.Riggi, C.Spitaleri, and D.Vinciguerra, Phys. Rev. C **21**, 1104 (1980).
[47] A. M. Mukhamedzhanov, Phys. Rev. C **84**, 044616 (2011).
[48] A. M. Mukhamedzhanov, L. D. Blokhintsev, B. F. Irgaziev, A. S. Kadyrov, M. La Cognata, C. Spitaleri, and R. E. Tribble, J. Phys. G: Nucl. Part. Phys. **35**, 014016 (2008).
[49] A. Tumino, C. Spitaleri, A. Mukhamedzhanov, G. G. Rapisarda, L. Campajola, S. Cherubini, V. Crucilla, Z. Elekes, Z. Fueloep, L. Gialanella, M. Gulino, G. Gyuerky, G. Kiss, M. La Cognata, L. Lamia, A. Ordine, R. G. Pizzone, S. Romano, M. L. Sergi, and E. Somorjai, Phys. Rev. C **78**, 064001 (2008).
[50] M. La Cognata, C. Spitaleri, O. Trippella, G. G. Kiss, G. V. Rogachev, A. M. Mukhamedzhanov, M. Avila, G. L. Guardo, E. Koshchiy, A. Kuchera, L. Lamia, S. M. R. Puglia, S. Romano, D. Santiago, and R. Spartá, Astrophys. J. **777**, 143 (2013).
[51] F.Strieder, C.Rolfs, C.Spitaleri, and P.Corvisiero, Naturwissenschaften **88**, 461 (2001).